# Constitutive response and failure progression in digitally fabricated (3D printed) concrete under compression and their dependence on print layer height

Sooraj A. O. Nair<sup>1</sup>, Avinaya Tripathi<sup>2</sup>, Narayanan Neithalath<sup>3</sup>

#### Abstract

Among the several geometry and process-related characteristics that determine the ultimate product quality of 3D printed concrete, one that has gained considerable importance is the height/thickness of the individual layers. Layer height dictates the number of interlayer interfaces, and influences the properties of the layer and the interfaces (both interlayer and inter-filament), for a given mixture and printer characteristics. This paper examines the influence of layer height on the constitutive response and failure of 3D printed concrete specimens under compression, investigated along the direction of layer build-up (or perpendicular to the layer interfaces), which is the dominant plane of loading in 3D printed walls and columns. Plain and steel fiber-reinforced wall elements with two different layer heights (7.5 mm and 15 mm) are printed, from which cylindrical and prismatic specimens are extracted and tested. The uniaxial compressive strength is seen to decrease with increasing layer height. The constitutive relationships of the specimens with different layer heights, along with volumetric strains, enable the extraction of crack initiation stress and unstable crack propagation stress, which are influenced by layer height and the presence of fiber reinforcement. The unstable crack propagation stress is lower than the peak stress, and it decreases with increasing layer height. Digital image correlation (DIC) is used to demonstrate the dominant effect of inter-filament interfaces on the crack propagation response and resultant failure.

**Keywords:** Concrete 3D printing; constitutive response; layer height; digital image correlation; fiber reinforcement

<sup>&</sup>lt;sup>1</sup> Senior Researcher, USG Corporation, Libertyville, IL (formerly, Graduate student, School of Sustainable Engineering and Built Environment, Arizona State University, Tempe AZ)

<sup>&</sup>lt;sup>2</sup> Graduate student, School of Sustainable Engineering and Built Environment, Arizona State University, Tempe AZ 85287

<sup>&</sup>lt;sup>3</sup> Professor, School of Sustainable Engineering and Built Environment, Arizona State University, Tempe AZ 85287; e-mail: <u>Narayanan.Neithalath@asu.edu</u>

#### 1 Introduction

3D printing (also referred to as additive or digital construction) of concrete is an advanced construction methodology that has gained widespread acceptance recently [1,2]. Extrusion-based printing has been commonly adopted as the digital fabrication method for concrete, both in academic studies as well as several full-scale structures that has been printed and initiated into service [3]. In the extrusion-based printing method, concrete (or mortar) is laid layer-by-layer by a printer through a nozzle, allowing for geometric flexibility wherein non-linear and optimized geometries (for structural and/or functional requirements) are easily achieved. This layer-by-layer, form-and-vibration free construction necessitates unique rheological properties for the printable concrete, which are attained through careful control of powder materials (cement, cement replacement materials, fillers etc.), and the use of water-reducing, accelerating, and/or viscosity-modifying admixtures [4–7]. The material characteristics, layering and layer characteristics (layer height and width, orientation), and the process parameters (print speed, path and time, nozzle standoff distance etc.) are influential in the early- and later-age properties of 3D printed concrete, contrary to conventional concrete where material characteristics alone are predominantly responsible for the properties [7–10]. Another significant challenge in 3D printed concrete is to incorporate reinforcement during printing. Several studies have attempted to use external and internal reinforcements, including mesh, chain, wire, and discrete steel bars [11-13]. A direct reinforcing method for 3D printed concrete is to incorporate metallic fibers in the mixture, which contributes to fresh print stability as well as post-peak ductility in the hardened state [14,15].

3D printed concrete specimens are generally known to have relatively weaker interlayer and inter-filament interfaces, thus greatly influencing their cracking and failure behavior [16], which renders the mechanical responses in all the directions not essentially being the same [8,17,18]; i.e., the assumption of material being isotropic in structural and stress analysis, as is usually considered for traditional concrete elements, is not strictly valid. It is reported that the strength is typically higher when compressed in the direction of the print, though contrary results can also be found [18–21]. Tests carried out on elements with different print orientations (e.g., staggered layers, curved filaments) have suggested that patterns with directional resistance to the load case, or patterns which improve the infill packing (e.g., staggered layers) show better mechanical performance [22–24]. A recent work by the authors have demonstrated appreciable property enhancement through a combination of material design and orientation changes [23]. However, the influence of layer heights on mechanical properties of 3D printed concretes needs further attention, especially given that: (a) layer heights and the resulting number of interlayer and inter-filament interfaces exert a combined influence on the measured mechanical properties [10] and failure propagation, and (b) layer height is a frequently altered design parameter to achieve desired levels of construction productivity.

It has also been shown that the fibers (especially those longer than the layer height) likely improve interlayer bonding and expectedly, the performance under flexure [10,18]. Relationships between the fiber length, layer height, and the changes in flexural properties have also been arrived at [10]. The synergistic effects of layer height, fiber type, length and volume fraction, and printing parameters could also result in adverse effects such as weaker interlayer interfaces and increased porosity [10], culminating in detrimental effects on mechanical properties when compared to non fiber-reinforced counterparts [25–27]. Hence, this paper investigates the influence of layer height on the compressive stress-strain response of 3D printed concrete elements with and without steel fiber reinforcement. The use of metallic fibers is emphasized here to enable better properties, especially with respect to crack resistance and ductility, which have been demonstrated under flexure in our previous work [10]. Two different layer heights and two different specimen geometries are used for plain and steel fiber-reinforced 3D printed specimens, and the constitutive response and failure propagation under compression are studied. Non-contact digital image correlation (DIC) and ultrasonic pulse velocity (UPV) techniques are also used to provide further information on the response of these specimens when subjected to uniaxial compression. The results provide insights into the effect of layer height on the compressive stress-strain response of printed mortars, the mechanisms of crack propagation in cylindrical and prismatic specimens, and the influence of small amounts of fiber incorporation on the compressive response. The study provides insights on failure of such layered systems under compression and helps to formulate recommendations towards proportioning of appropriate mixtures for use in concrete 3D printing, as well as failure patterns of interest when considering the structural behavior of the printed element.

# 2 Experimental Program

#### 2.1 Materials and mixtures

Type I/II Ordinary Portland Cement (OPC) conforming to ASTM C 150, fine limestone (L) powder conforming to ASTM C 568, and medium sand (M) conforming to ASTM C 778 are used as the primary mixture ingredients. The chemical and physical properties of the constituents are given in Table 1. Brass-coated straight steel fibers, 13 mm long and 200 μm in diameter (specific gravity of 6.8 g/cc), and a polycarboxylate ether-based superplasticizer were used in the mixtures. The proportions of the printable mortars (plain and fiber-reinforced) containing 50% sand (by mass of the binder) were derived from the authors' earlier work [10,28] and are shown in Table 2. The water and admixture dosages were adjusted to ensure adequate extrudability and buildability (i.e., a structuration rate, A<sub>thix</sub>, that explains the time-dependent change in yield stress, of ~ 60 Pa/min, and an open time of up to 1.5 h that enables a buildability of ~400 mm for a 25 mm thick wall [29]). The values thus obtained were kept unaltered for all the

experiments. The mortar mixtures were 3D printed and cured for 28 d before subjecting them to compression testing.

Table 1: Composition and properties of the mortar constituents.

Components of the binders	Chemical composition (% by mass)							d <sub>50</sub>	Specific
	SiO <sub>2</sub>	Al <sub>2</sub> O <sub>3</sub>	Fe <sub>2</sub> O <sub>3</sub>	CaO	MgO	SO <sub>3</sub>	LOI*	(µm)	gravity
OPC	19.60	4.09	3.39	63.21	3.37	3.17	2.54	11	3.15
Limestone (L)	CaCO <sub>3</sub> > 99%						1.5	2.70	
Medium sand (M)	SiO <sub>2</sub> > 99%					600	2.40		
*Loss on ignition									

Table 2: Mortar mixture proportions.

	Mass fraction of ingredients				Water-to-powder	Superplasticizer	
Mixture ID	OPC	Limestone (L)	Sand (M)	Steel Fiber (F)§	ratio (w/p), by mass	(% by mass of binder)	
L <sub>30</sub> -sM	0.35	0.15	0.50	-	0.35	0.25	
L <sub>30</sub> -sM-f	0.35	0.15	0.50	0.27	0.35	0.35	

§Percentage by volume of the mixture. This is a low fiber volume fraction. Higher volumes of fibers interfere with printability; however significant alteration of the mixture design has enabled fiber volume fractions of upto 2%, for ultra-high performance printed mixtures. The use of smaller size fibers can also enable inclusion of a higher volume fraction without compromising the extrudability and printability.

# 2.2 3D printing of mortars

The plain and fiber-reinforced mortars were printed using a gantry 3D printer, capable of printing structures roughly 2 m  $\times$  2 m  $\times$  2 m in size, as detailed in [10]. The printer is outfitted with a feed system through which the material was placed layer-by-layer to build vertical walls shown in Figure 1(a). Wall elements of  $330 \times 330 \times 80$  mm in size were printed with two different layer heights of 7.5 mm and 15 mm, as shown in Figures 1(b-c). The nozzle travel speed was maintained at 50 mm/s, with the stepper calibrated at a flow rate of about 8.5 or 17 mL/s for layer heights of 7.5 mm and 15 mm respectively. A circular nozzle diameter (ND) of 20 mm was used to print filaments at the specified layer heights (note that, while the centerline of the filaments are only 20 mm apart as per the design, the extrusion rates as well as the rheology of the mixture resulted in the filaments spreading wider, which indirectly helps reduce the inter-filament voids; individual filaments printed at the chosen extrusion rate and layer heights when measured were observed to be  $\sim$ 22 mm wide). Multiple inter-filament interfaces were also thus introduced. The layer heights were 0.375 and 0.75 times the nozzle diameter, which also helped in providing some compaction to the filaments while being printed, thereby reducing the inter-filament and inter-layer voids. While in the past, we have printed slabs from which beams were cut for flexural property characterization, in this study the specimens were printed in a vertical configuration (such as columns and walls, which are currently the most common

applications of 3D printed concrete elements) to induce the effects of overhead pressure on layers below them.

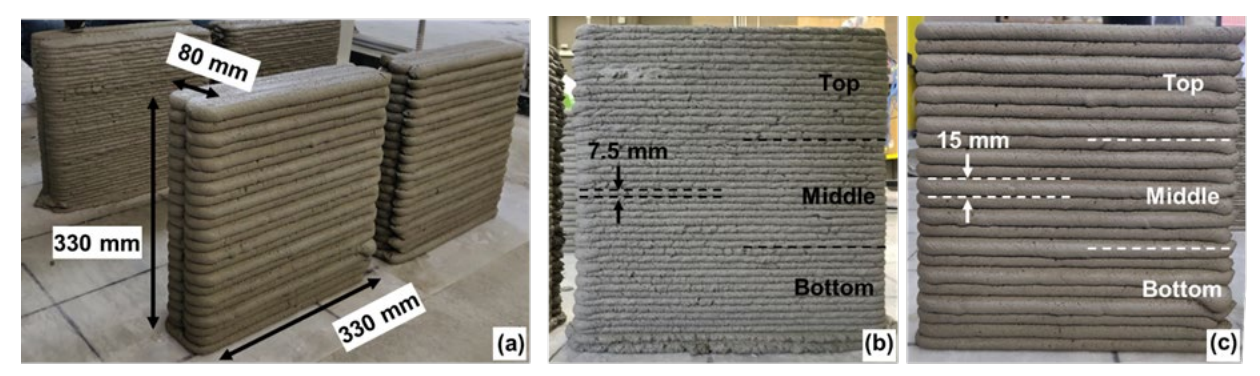


Figure 1: (a) Printed wall elements with the specified dimensions, (b) specimen printed with a layer height of 7.5 mm, and (c) specimen printed with a layer height of 15 mm. The regions marked top, middle, and bottom were used to obtain specimens for the compression tests from these zones.

# 2.3 Specimen preparation for compression testing

The 3D printed specimens were cut into three sections marked top, middle, and bottom, as shown in Figures 1(b-c). These specimens were cut and cored to extract prisms and cylinders of specified dimensions, as shown in Figure 2(a). The coring of the cylinders was done slowly (at a rate of 11.62 mm/min), as shown in Figure 2(b), with water feed to mitigate heat build-up. The cylindrical cores were 50 mm in diameter and were cut flat on the edges to obtain an overall specimen height of 100 mm (thus maintaining an aspect ratio of 2 for compression testing). A typical cylindrical specimen is shown in Figure 2(c) which is further prepared for testing by using a thin, flexible rubber latex membrane as a band at the center of the cylinder to position the radial extensometer. Figure 2(d) shows a typical prismatic specimen with a cross-section of  $50 \times 50 \text{ mm}$  and a height of 100 mm. The cylindrical and prismatic specimens were speckled for digital image correlation (DIC) analysis, the details for which are provided later.

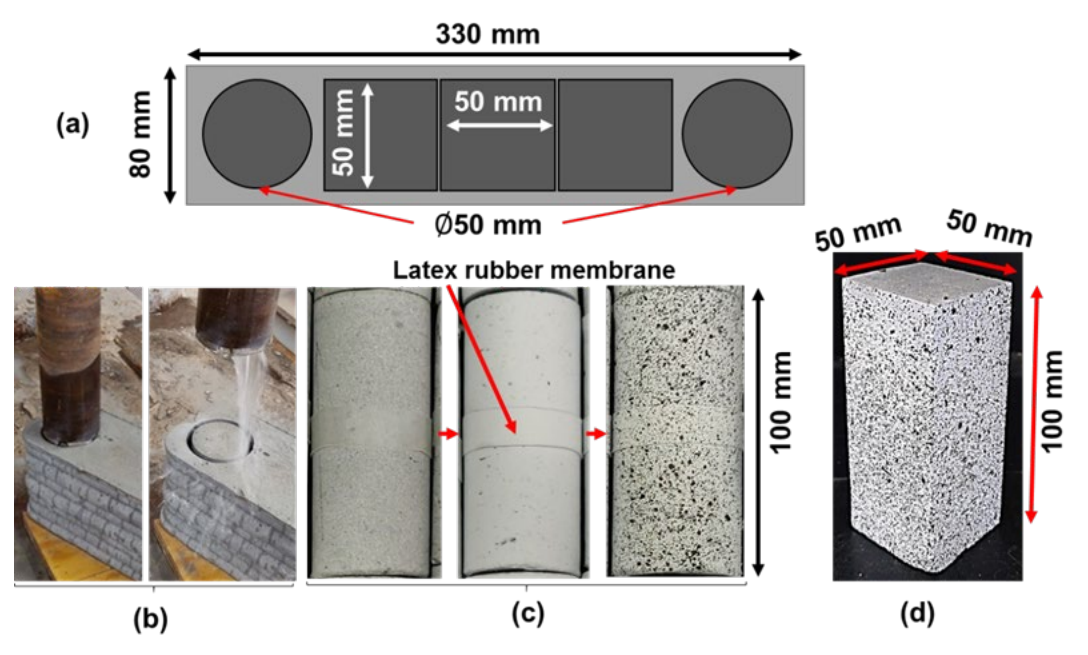


Figure 2: (a) Schematic showing locations and direction of specimen extraction from the vertical printed walls, (b) coring cylinders from the prints, and (c-d) speckled and ready-to-test cylindrical and prismatic specimens.

# 2.4 Compression testing

The cored cylinder specimens were tested in compression as shown in Figure 3(a), in accordance with a procedure used by the authors to determine the stress-strain (axial and radial) response of ultra-high performance concretes [30]. The specimens were tested using a servo-controlled universal testing machine (SBEL CT-110-S) with a capacity of 489 kN (110,000 lbf) to extract the stress-strain response of the cylinders. The specimens were placed in the test machine such that the top platen of the machine coincided with a layer on the top region of the corresponding zone of the printed specimen. In other words, for the cored specimens, the layer that was on the top in a certain zone (top, middle, or bottom in Figure 1) remained at the top while being tested also. Here, the loading platens in contact with the specimen contained internal transducer assemblies (see Figure 3(b)) to determine the ultrasonic pulse velocity (UPV). The test was run in two stages: (i) initial load-controlled stage at a rate of 1500 N/m (~330 lbf/min) until 22 kN (~5000 lbf), and (ii) axial displacement-controlled stage at a rate of 0.0375 mm/min (corresponding to 0.03% strain per min) until a 60% load reduction in the post-peak region [30]. A GCTS ULT-200 unit was used to control the set up to measure the dynamic evolution of elastic properties using the P-wave (compression wave) and S-wave (shear wave) velocities measured continuously during loading [30,31]. Proper contact was ensured by applying an electrode gel at both ends to maintain continuous and smooth stress wave propagation. The P-wave and S-wave arrival times were used to non-destructively measure the elastic modulus (E) and Poisson's ratio (v) for the specimens [32,33]. The time of flight is taken at the onset of the rise in signal amplitude at the receiving transducer. Since the S-waves could be impacted by local reflected waves and appear as noise in the received signal, the first arrival time was taken as the point where a significant change in the signal amplitude was observed [30,34]. The wave velocity is calculated based on the transducer spacing (specimen length) and the signal arrival time. The elastic constants (E and  $\nu$ ) of the material were calculated from the P- and S- wave velocities ( $V_p$  and  $V_s$ ), and the specimen density ( $\rho$ ) using the following relations [35,36].

$$\nu = \frac{V_p^2}{V_p^2 - V_s^2}$$
 Eq. 1

$$E = V_p^2 \cdot \rho \cdot \frac{(1+v)(1-2v)}{(1-v)}$$
 Eq. 2

Since the specimen undergoes axial and radial deformation under compressive loading, a dynamic correction factor ( $F_{CD}$ ) was used to account for the change in transducer spacing during the test (although this dimensional compression is relatively small).  $F_{CD}$  is a function of the engineering strain ( $\varepsilon_e$ ) and is shown in Equation 3. The corrected length, shown in Equation 4, is used to obtain the wave velocity at different stress or strain levels [35,36].

$$F_{CD} = (1 + \varepsilon_e)$$
 Eq. 3

$$L_{corrected} = L_{original} * F_{CD}$$
 Eq. 4

# 2.5 Digital Image correlation for visualization of strain profiles

Digital image correlation (DIC) is used as a non-contact means to acquire the surface strain fields in the specimen during compression testing [37]. The DIC technique determines the horizontal and vertical displacement fields in the analysis region by minimizing the correlation coefficient computed between the subset of images in the deformed and the undeformed states [38,39]. The use of DIC necessitates a diligent and rigorous approach to ensure the accuracy of results – while the acquisition of full-field surface displacements or strains and their spatio-temporal representation is a distinct advantage, sample preparation and measurement conditions need to be carefully chosen [40–42]. The overall compression test setup with DIC is shown in Figure 3(a), which included two charge-coupled device (CCD) cameras (Point Grey Grasshopper<sup>TM</sup> 5-megapixel cameras) focused on a speckled area of interest on the surface of a cylinder (or on two surfaces of a prism, in some cases as discussed later) and illuminated by high-intensity flood lights. The cameras were calibrated using a calibration plate at the correct aperture and focus adjustments to enable tracking of the speckle pattern across the images. The data acquisition units acquired images at a frequency of 2 Hz, which was later synchronized with the time-stamped load-displacement data from the testing

machine. The DIC data was used to isolate the actual vertical displacement of the specimen under compression, and to track the crack initiation and propagation stages in layered specimens, using Correlated Solution Inc's VIC-3D<sup>TM</sup> software. Figure 3(c) shows a typical DIC strain field after post-processing the images for cylinders subjected to compression testing. The process of using surface displacement fields obtained from DIC to determine the Lagrangian principal strain fields has been described in detail elsewhere [43,44].

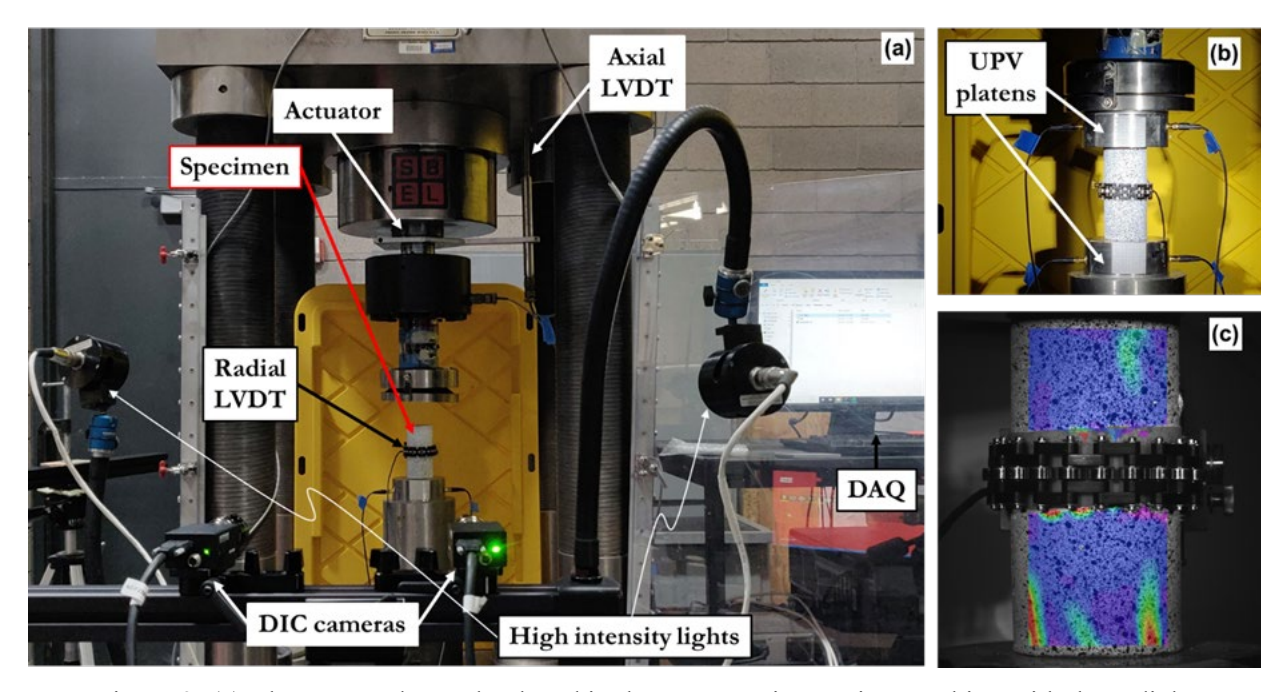


Figure 3: (a) The prepared sample placed in the compression testing machine with the radial extensometer positioned near the center, and the 3D-DIC setup in position, (b) specimen during testing with the UPV platens in position at the top and bottom faces, and (c) typical strain profiles extracted using DIC close to the peak load.

Since the field of view is obstructed due to the radial extensometer, and the possibility of cracking (and subsequent failure) to occur in the direction of the cameras is relatively lower in cylinders, which impedes the ability to obtain crack propagation information, prismatic specimens were also tested using 2D DIC, as shown in Figure 4(a). Each camera was placed perpendicular to the adjacent speckled faces of the prism and focused to track the speckle pattern. This camera placement method allows for the capture of cracks that are likely to initiate in one of the orthogonal directions. Typical post-processed image data showing the principal strain fields are shown in Figures 4(b)-(c).

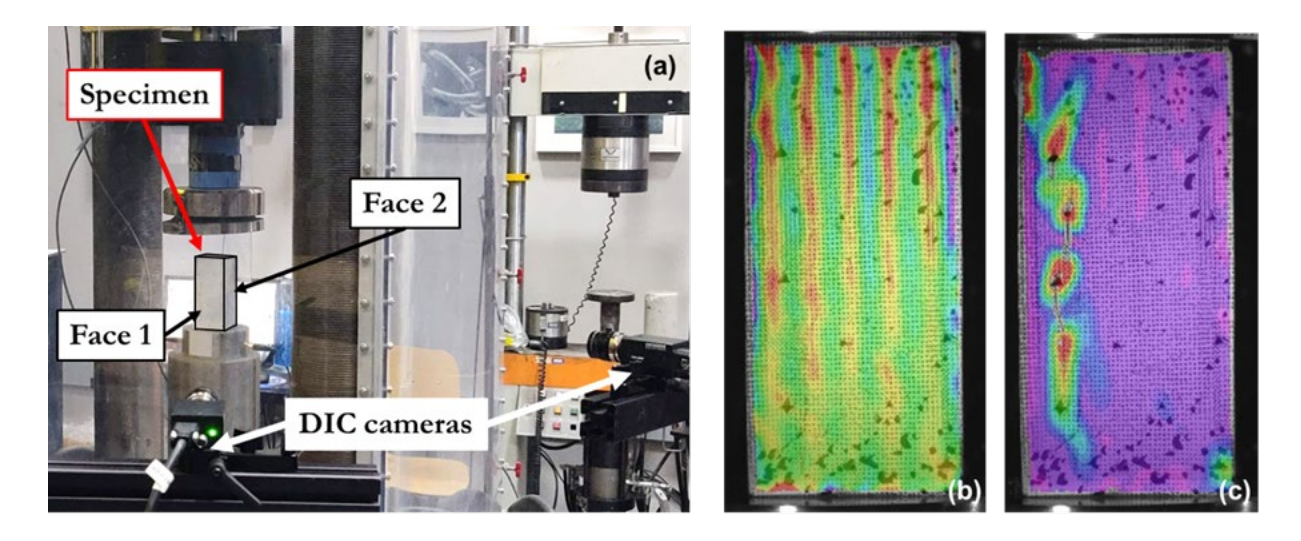


Figure 4: (a) Prismatic specimens subjected to DIC with cameras focusing on two orthogonal faces, and (b-c) typical strain profiles on orthogonal faces 1 and 2 respectively

#### 3 Results and Discussions

# 3.1 Compressive strength as a function of layer height

Compressive strengths of the samples were determined separately for samples extracted from different locations, viz., top, middle, or bottom of the printed walls (see Figure 1(c)). The average compressive strengths for samples extracted from different locations in the print were compiled into one single average compressive strength since no discernible trend was noted between strengths from the three different zones. Furthermore, this simplifies the analysis and interpretation of material properties. The average compressive strengths of the tested cylinders (plain and fiber-reinforced) obtained from specimens printed with two different layer heights are shown in Figure 5. 28-day compressive strengths > 50 MPa were obtained for the selected mortars. In general, the compressive strengths of 3D printed specimens were lower than those of companion mold-cast specimens, and the differences ranged between 5 and 20% depending on the layer height. The average compressive strengths for the plain and fiber-reinforced specimens are found to be lower when the layer height is higher. While the plain mortar specimens showed a reduction in average compressive strength of about 15%, the fiber-reinforced specimens showed a drop of about 25% when the layer height was doubled from 7.5 mm to 15 mm. This is primarily because an increase in layer height, while reducing the number of interlayer interfaces, likely results in less compact inter-layer interfaces. This, coupled with the lack of aggregate interlock in layered construction [45] results in a lower strength. It was also shown that, due to the vertical nozzle pressure (which has been shown to be ~50% higher when a layer height of 5 mm is used, as opposed to 15 mm [10]), the overall porosity near the layer interfaces is much lower when lower layer heights are used [10], which is also true for the bulk portion of the layer. The compactness of the interfaces is thus more influential than the number of interfaces when the compressive

behavior is considered, as noticed from the results shown in Figure 5. The interplay between the number of interfaces and their compactness becomes more critical under loading cases where disjoining forces are more dominant early on in the testing stage (e.g., tension and flexure). A small vertical pressing force (which is determined to be in the range of 1.7-2.1 kPa for 15 mm layer height [29]) arising out of a non-zero nozzle standoff distance during printing is found to beneficial towards the compressive properties of 3D printed concrete specimens, which has also been explained elsewhere [10,46].

When a small volume of steel fibers is added to the mixture, the trend with respect to layer height remains the same as that for the plain mixture. A closer look at Figure 5 shows that, for a layer height of 15 mm, the plain and fiber-reinforced mortars demonstrate the same strengths. However, the fiber-reinforced mortar shows ~10% higher average strength for a lower layer height. It must be noted that a layer height of 7.5 mm is lower than the fiber length (13 mm), and thus the fibers may not be contained entirely within the layer if they are not oriented exactly parallel to the printing direction. In general, short fibers coming out of the nozzle preferentially align themselves in the direction of printing, but visual observations have shown that longer the fiber, their orientation along the height of the layer is not 0°. The fibers could also scratch the surface while printing, creating interlayer defects. However, the possibility that some of the fibers could "bridge" the interfaces because they are longer than the layer height, is a probable cause for the increased strength for the smaller layer height specimens seen in Figure 5. This is corroborated by X-ray tomography studies that show fibers that are longer than the layer height are oriented at a higher angle to the horizontal (printing direction) than shorter fibers, potentially resulting in interlayer reinforcing. Moreover, the fiber-reinforced mixture here used an increased amount of superplasticizer to ensure easier placement, which also could have helped to reduce minor defects during printing.

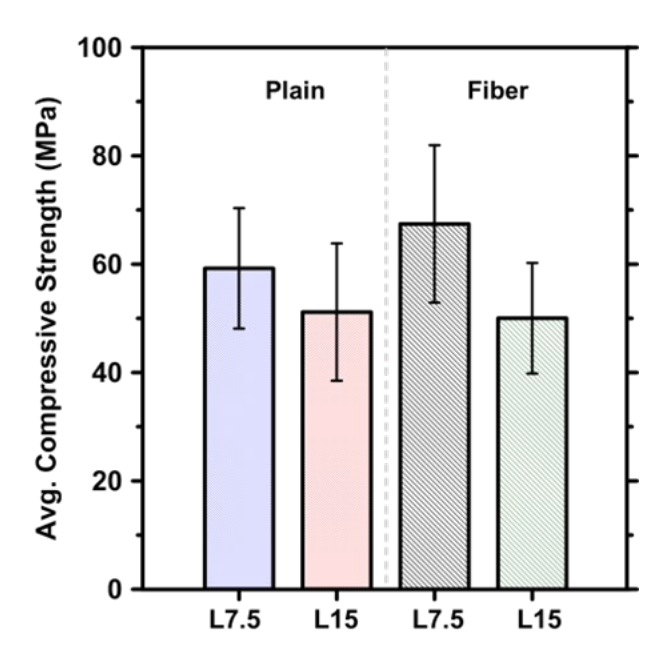


Figure 5: Average compressive strengths of plain and fiber-reinforced mortars printed at layer heights of 7.5 and 15 mm. The standard deviations reported here correspond to results from 9 cylinders tested, corresponding to top, middle, and bottom locations of the printed wall.

# 3.2 Constitutive response of plain and fiber-reinforced 3D printed specimens and extraction of critical stress states as a function of layer heights

Figure 6 shows representative plots of unconfined compressive stress versus axial and radial strains for cylindrical plain and fiber-reinforced mortar specimens. The stress-axial strain response shows that the plain mortar specimens are brittle, as expected. In contrast, the fiber-reinforced specimens show an initial drop in stress after the peak load, after which a strain-softening response is noted. The initial drop in stress can be attributed to a relatively small volume fraction of fibers used (0.27%) here. Our past experience shows that a fiber volume fraction > 0.5% results in a gradual strain softening behavior instead of a sharp drop at the peak, which is attributed to the ability of the discrete fibers to carry some load. Here, the strainsoftening behavior is noted to start at around 40-50% of the peak stress in the post-peak region. The very small stress rebound observed for the fiber-reinforced specimens shortly after the peak load shows that there is not enough number of fibers to engage in load transfer until the crack extends further (due to the fibers being spaced further apart because of the low volume fraction). Even beyond an axial strain of ~0.6% (2 times higher than the maximum strain capacity generally attributed to concrete in structural design), approximately 40% of the peak strength is retained irrespective of the layer heights. Since the volume fraction of fibers used in these mixtures is low, the post-peak ductility is also lower. Note that, with changes in fiber volume fraction, the stress-strain response will change, but the general trends described here are expected to be retained. The axial strain at peak stress is relatively higher for a lower layer height, probably attributed to the fact that a higher number of layer interfaces (when layer height is smaller) could result in more energy dissipation during crack propagation under compressive loading, aided by a potential increase in crack path tortuosity. Our previous work [9] has shown through DIC that cracks in layered 3D printed systems propagate into the interface and into the next layer; and thus, with more interfaces as in the case of a lower layer height specimen, there is more energy dissipation. Even though the interface for a higher layer height specimen is expected to be slightly more compliant than that for a lower layer height specimen, the difference is not significant so as to consistently drive the crack along the interfaces. This work also showed that the critical strain energy release rate was higher when the layer height was lower. Thus, decrease in crack growth rates as the layer height decreases can be considered to be a mechanism that enhances the strain capacity at peak in lower layer height specimens.

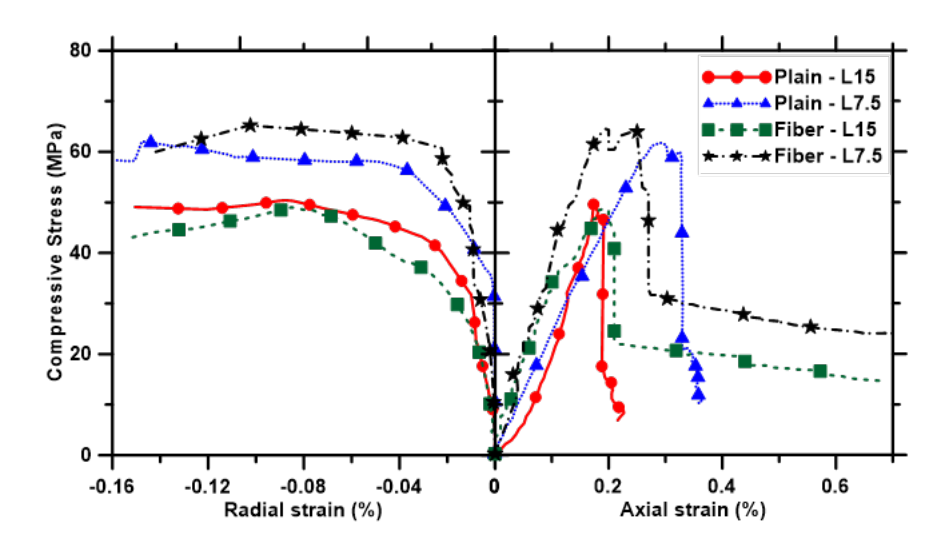


Figure 6: Representative stress-strain profiles extracted for plain and fiber-reinforced specimens for layer heights of 7.5 and 15 mm. Stress is plotted against axial and radial strains. Rather than averaging the stress-strain curves for at least 3 specimens tested for each of these cases, representative curves are shown.

Representation of axial stress as a function of both the axial strain and the radial strain can be deconvoluted to extract stresses corresponding to different stages of pre-peak crack propagation, similar to observations made elsewhere [30,47]. Four distinct phases in the pre-peak response have been identified, followed by a sudden failure or a post-peak response, depending on the level of ductility of the material. The different phases in crack propagation and their determination are shown in Figure 7. In Phase I, pre-existing microcracks in the sample close under compressive stresses and can be considered to extend to about 0.001% radial strain. Once the existing cracks are closed, the material behaves in a linear elastic fashion, labeled as Phase II, which enables the extraction of material parameters (i.e., Young's modulus and Poisson's ratio). The linear region is generally limited to an axial strain corresponding to 40-60% of the peak stress (N.B: in order to exactly account for the end of the elastic region, a crack initiation stress is defined later). Damage accumulation and formation of new cracks is considered to begin at the end of the elastic regime, which marks the beginning of Phase III which is denoted as the stable crack growth regime. Crack initiation is generally difficult to determine from axial stress-strain curves, especially in samples that contain microcracks. The beginning of Phase III corresponds to crack initiation under compressive stress, and the corresponding stress is called crack initiation stress ( $\sigma_{ci}$ ). Crack initiation is determined by relating the crack volumetric strain and the axial strain. The crack volumetric strain ( $\varepsilon_{v,cr}$ ) is calculated from the total volumetric strain ( $\varepsilon_v$ ) and its elastic component ( $\varepsilon_{v,e}$ ) as shown in Eqs. 5-7 ( $\varepsilon_{axial}$  is the axial strain,  $\varepsilon_{radial}$ is the radial strain, v is the poison's ratio, and E is the elastic modulus corresponding to the linear elastic region in the axial stress-strain curve). Crack initiation is the point where the crack volumetric strain starts

to deviate from zero in the axial strain-volumetric strain relationship in Figure 7 (note that the linear elastic stage corresponds to the total volumetric strain being just from the elastic contribution, and thus the crack volumetric strain is zero during the linear region). For the case shown here, this value is about 50% of the peak stress. The axial stress level corresponding to the beginning of Phase IV, which is the unstable crack growth phase, is indicated by the location where the total volumetric strain reversal occurs, i.e., the contraction levels starts to drop. The stress corresponding to this reversal in  $\varepsilon_{\rm v}$  is denoted as the crack damage stress ( $\sigma_{\rm cd}$ ), thus termed since stresses exceeding this value results in failure under permanent loads. In this phase, the rapid increase in crack volumetric strain results from an increase in crack density. This stress should ideally be regarded as the true (albeit conservative) strength of the material, with any further increase in strength being a result of the temporary strain hardening effect [47]. This phase ends at the peak stress ( $\sigma_p$ ), corresponding to the point where volumetric strain drops back to zero.

$$\varepsilon_{\rm v} = \varepsilon_{\rm axial} + 2\varepsilon_{\rm radial}$$
 Eq. 5

$$\varepsilon_{\rm v,e} = \frac{1-2{\rm v}}{E} \left(\sigma_{\rm axial}\right)$$

$$\varepsilon_{v,cr} = \varepsilon_v - \varepsilon_{v,e}$$

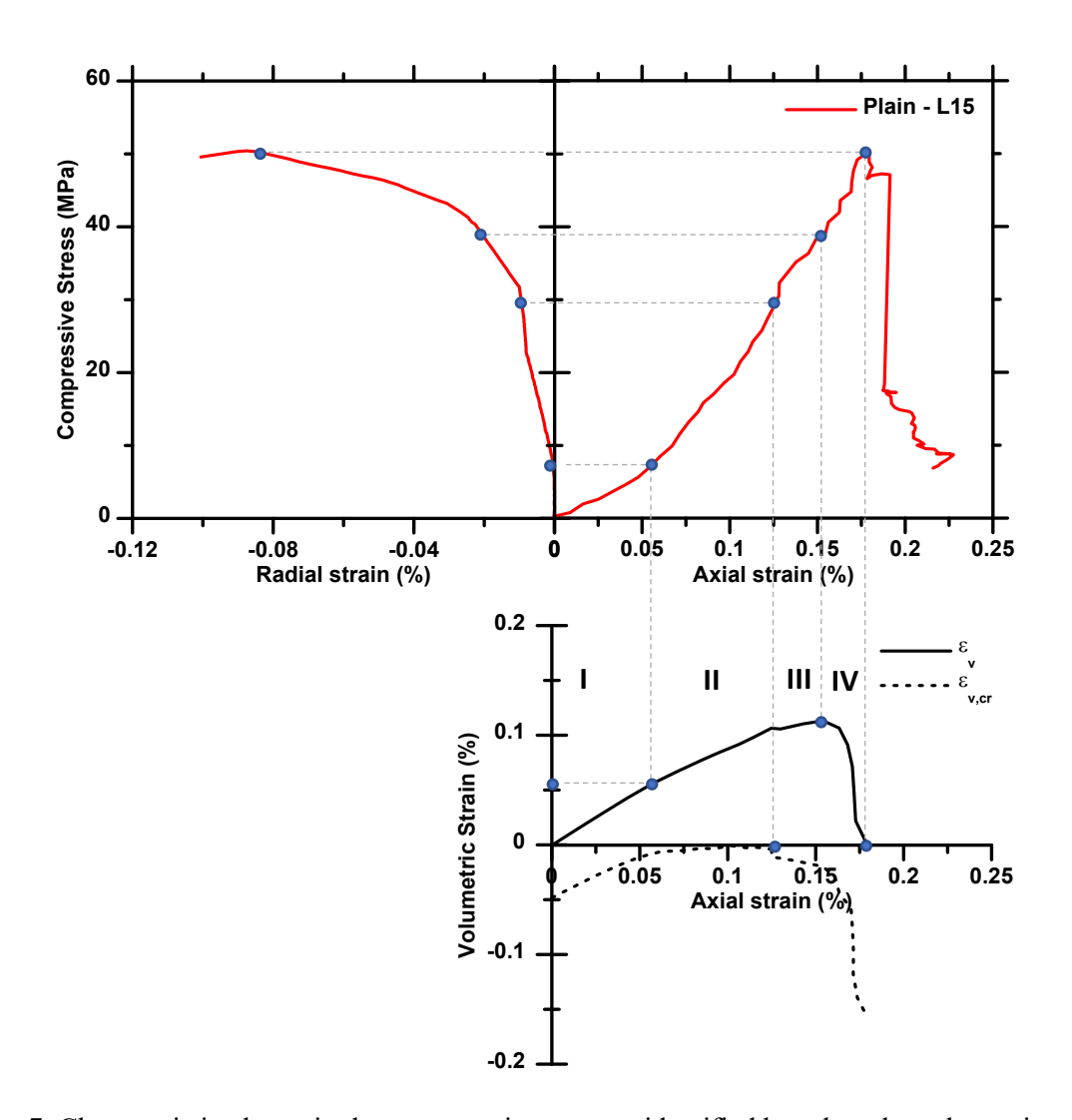


Figure 7: Characteristic phases in the stress-strain response identified based on the volumetric strains demonstrating phase transition points including crack initiation ( $\sigma_{ci}$ ), crack damage ( $\sigma_{cd}$ ), and peak ( $\sigma_p$ ) stresses. The solid line in the axial strain-volumetric strain plot corresponds to the total volumetric strain, and the dotted line, to the crack volumetric strain

Figure 8 depicts the crack initiation, crack damage, and peak stresses for the plain and fiber-reinforced specimens printed using two different layer heights. For both the plain and fiber-reinforced concretes, crack initiation occurs at a lower stress when the layer height is higher. This can be attributed to a weaker matrix in the case of a higher layer height specimen because of the differences in consolidation provided by the nozzle overburden pressure when printed with a non-zero standoff distance. More number of denser (and thus stronger) interlayer interfaces in smaller layer height specimens results in higher energy dissipation (which has been shown in our earlier work [10]), thus demanding higher stress for further crack propagation, which accounts for the higher crack initiation and damage stresses for such cases as shown in Figure 8. While the crack damage and peak stresses are different only by ~10% for the plain and fiber-reinforced lower layer height specimens, the corresponding difference is ~20% in the case of larger layer heights. If

 $\sigma_{cd}$  is considered as the true strength, then the difference induced by an increase in layer height is significant. Stable crack growth is noted to occur at 50-80% of the peak stress, and at ~80-95% of the peak stress, cracks coalesce and propagate in an unstable manner. Between plain and fiber-reinforced specimens, the effect of fibers is most notable in the crack initiation stress. For higher layer heights, the crack initiation stress is found to be lower for the fiber-reinforced specimens, possibly attributed to the fact that the fibers weaken the matrix through packing and wall effects [48,49], and are most likely to be predominantly aligned along the direction of printing, providing a statistically lower chance to arrest crack initiation. This is likely not an issue at lower layer heights because the fibers being longer than the layer height, are aligned more randomly, and could traverse layers as noted in x-ray tomography imaging. The detailed analysis using constitutive relationships that include both the axial and radial strains, and the use of volumetric strains to extract the critical stress states enable an in-depth understanding of the combined effects of fiber reinforcement and layer heights that simple determination of peak stresses or axial stress-strain relationships alone cannot provide. The use of varying fiber lengths and volume fractions could also shed more light into the compressive behavior, but that is beyond the scope of the current work.

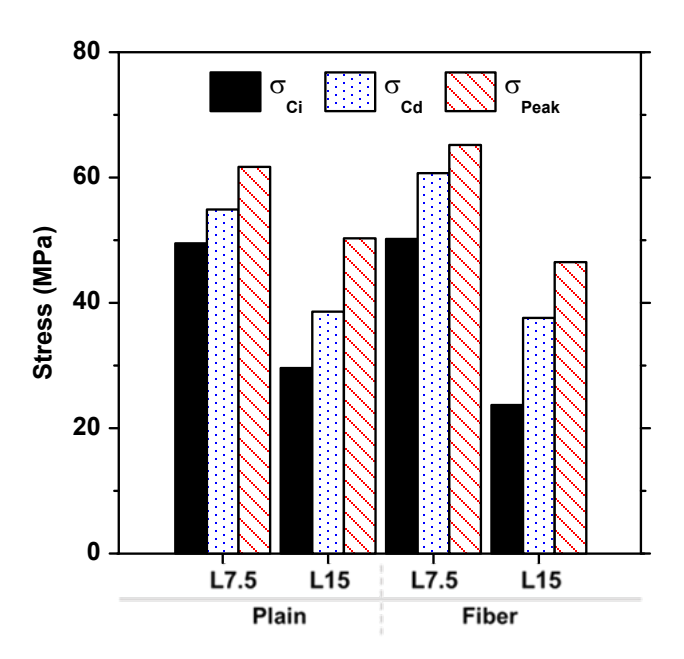


Figure 8: Critical stress states, viz., crack initiation ( $\sigma_{ci}$ ), crack damage ( $\sigma_{cd}$ ), and peak ( $\sigma_p$ ) stresses based on layer height and mixture type. The values are averaged from the 3 specimens for each of the cases tested under compression.

# 3.3 Elastic constants from stress-strain relationships and UPV

The experimental E and v values were estimated from the secant slope of the elastic region (between stress corresponding to -0.001% of radial strain to the crack initiation stress) in the stress-strain response. The dynamic elastic constants from UPV were deduced from the P-wave and S-wave velocities based on

Equations 1 and 2. The elastic constants determined using both the approaches are shown in Table 3. The dynamic elastic constants from UPV are calculated for the pre-peak (E<sub>UPV-initial</sub>, v<sub>UPV-initial</sub>) and close-to-peak regions (E<sub>UPV-peak</sub>, v<sub>UPV-peak</sub>). This corresponds to a low axial stress (~10 MPa) for the initial values, and close to failure or at an axial strain of ~0.2-0.3% for the final values. Poisson's ratios are also calculated at the same stress and strain levels as the moduli. The values of E and v at different stress levels are along expected lines – the stress wave-measured (dynamic) E values are higher than those of the experimentally measured (static) values [50]; and the values measured close to the peak load are lower [30] due to damage initiation and propagation. The velocities remained reasonably consistent throughout the test until close to the peak stress. The signal travel time is expected to be highest in the tested direction owing to the presence of weaker interfaces in printed specimens, as reported elsewhere [17]. Since the tests are done in the primary vertical print direction in this study, the specimens with a layer height of 15 mm show relatively higher signal arrival times when compared to those with a layer height of 7.5 mm, owing to the effect of lower nozzle pressure, and less compact layers and layer interfaces, even though the number of inter-filament interfaces is higher in the lower layer height specimens. The elastic moduli for the fiber-reinforced specimens were found to be slightly higher than those of the plain-printed specimens. While the small volume of fibers used is unlikely to result in a markedly higher stiffness, it is possible that the use of higher amounts of superplasticizer in the fiber-reinforced mixture (to ensure smoother placement in the presence of fibers) resulted in ensuring defect-free placement, as explained earlier. The Poisson's ratios determined from UPV, especially for the fiber-reinforced specimens are inconsistent; this is likely due to the need to use S-wave velocity for Poisson's ratio determination (since more reliable P-wave velocities are only needed for E determination, the moduli values are more reliable). S-wave velocities are somewhat more difficult to accurately determine in non-homogeneous samples such as steel fiber reinforced concretes because of the multiple wave scattering effects contributed by the fibers.

Table 3: Elastic constants for plain and fiber reinforced prints determined from quasi-static stress-strain relationships, and P- and S-wave velocities.

	Pla	ain	Fiber-reinforced		
	L7.5	L15	L7.5	L15	
Elastic Modulus (GPa)				_	
Eexperimental	21.3	26.7	31.2	32.8	
E <sub>UPV-initial</sub>	29.4	29.9	33	33.4	
$E_{\mathrm{UPV-peak}}$	27.2	28.4	30	27.8	
Poisson's ratio					
$v_{ m experimental}$	0.27	0.19	0.14	0.15	
$ u_{ ext{UPV-initial}}$	0.23	0.24	0.16	0.16	
$ u_{ ext{UPV-peak}}$	0.21	0.23	0.22	0.22	

# 3.4 Crack propagation patterns observed from DIC

The principal strain profiles obtained from 3D DIC on the tested cylinders for plain and fiber-reinforced specimens, respectively, are shown in Figures 9 and 10. The frames were extracted corresponding to different stages in compression, with the principal Lagrangian strains (×10<sup>-3</sup>) as the contour variable. Note that the images from left to right correspond to frames extracted in stable crack growth phase (Phase III), unstable crack growth (Phase IV), peak stress or failure, and post-peak at 60% residual stress respectively. Figures 9(a) and (b) show the DIC images for the specimen with layer heights of 7.5 mm and 15 mm (L7.5 and L15) corresponding to the four stages identified above. For the L7.5 specimen, slowly increasing principal strain with little to no visible strain concentration is noticed until the specimen is in the post-peak region where multiple cracks are seen to be propagating. Visible failure indications are not seen ahead of the post-peak region because the failure regions are out of the field of view as visually observed during the experiments. The maximum principal strains are found to increase about 2-5 times from stable to unstable crack growth and to peak stress, respectively. For the L15 specimen, the maximum principal strains are roughly similar to that for the L7.5 specimen at crack initiation but are significantly magnified for the unstable crack growth, peak, and post-peak stages as shown in Figure 9(b), resulting in overall lower peak load capacity. Here, strain concentrations are identified even during the stable crack growth phase, and the crack grows to >50% of the length of the specimen close to the peak stress. The strain concentration that is observed in the L15 sample during the unstable crack propagation stage results in the remaining areas of the specimen encountering relatively smaller strains. The crack traverse path is largely vertical as seen in Figure 9, providing confirmation to the earlier discussion that the cracks are largely driven across the interfaces (and not along the interfaces) for the chosen layer heights. The effects of increasing layer height on crack propagation under compression is amply evident from the DIC analysis.

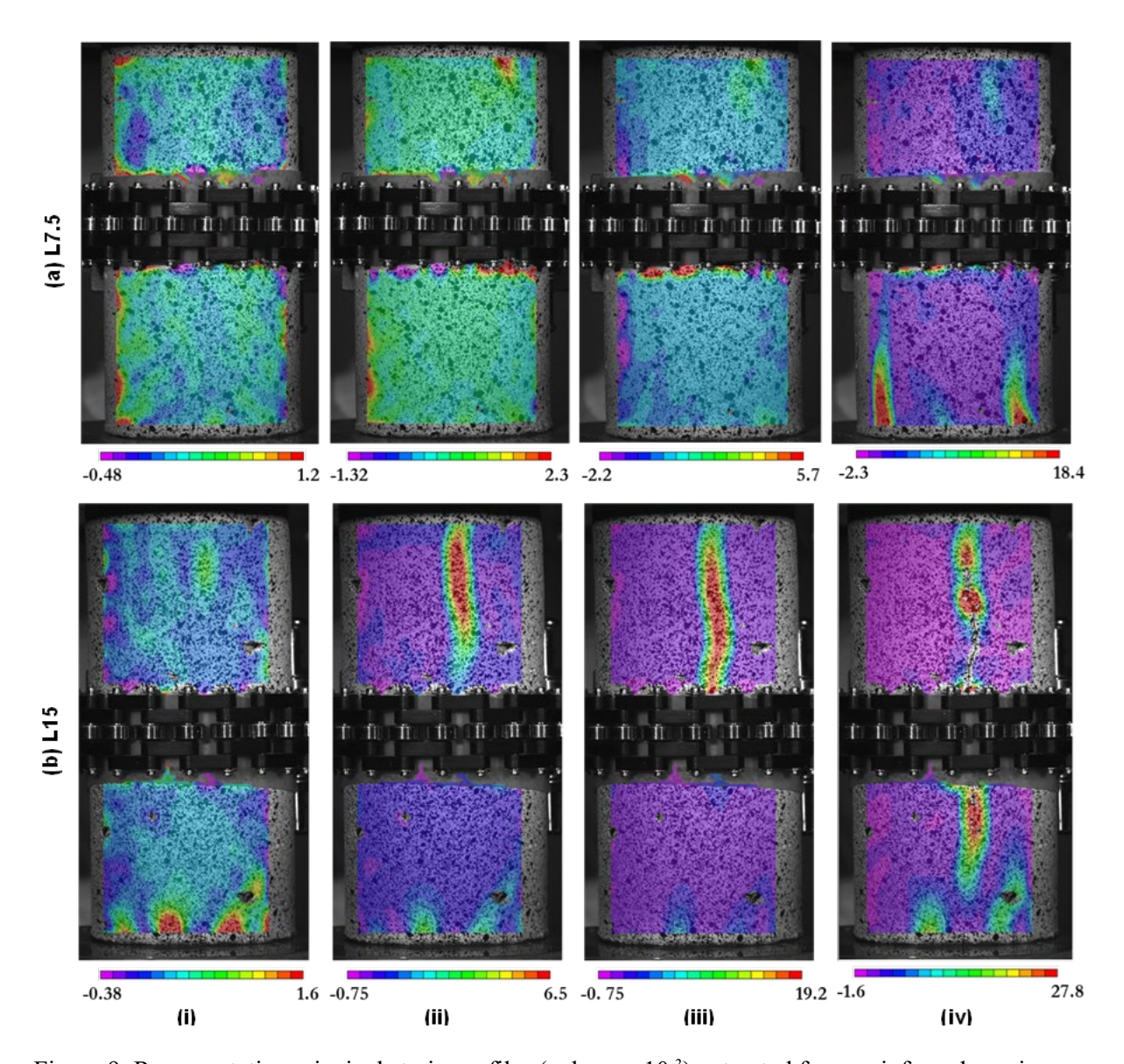


Figure 9: Representative principal strain profiles (values × 10<sup>-3</sup>) extracted for unreinforced specimens with layer heights of: (a) 7.5 mm, and (b) 15 mm at four stages (from left to right) – (i) stable crack growth, (ii) unstable crack growth, (iii) peak load, and (iv) 60% residual stress at post-peak.

Figures 10(a) and (b) show DIC analysis for the fiber-reinforced mortars of different layer heights. Some strain concentration is visible early on for fiber-reinforced mixtures, probably due to the defects created by the fibers as described earlier. Same trends in the maximum strain and average strains across the sample as noted in Figure 9 are seen here as well; however, the use of fiber reinforcement results in much larger strains in the sample, post-peak. For the L7.5 specimen, a significant crack is noticed outside the edge of the region of interest at the peak load, which results in a further grouping of cracks in that region during the post-peak stage. For the fiber-reinforced L15 specimen, the images show the presence of local and large interfilamentous gaps in the cored specimen, which are seen to act as crack nucleation points. The same

aspect could have occurred for the unreinforced mixtures in Figure 9, if the cored specimen encountered significant interfilamentous voids, thus alluding to the effect of local defects as a result of mixture or printing characteristics. We depict this specimen particularly to demonstrate the impact of an inherent flaw (which is statistically more likely on multi-filament 3D printed specimens with a higher layer height) on crack propagation. Local strain concentration is observed during the stable and unstable crack growth phases, which traverses the entire specimen at the peak load. Here, the maximum principal strains at peak are similar to that of the unreinforced L15 specimen, and the average strains are higher, attributable to the strain concentration that resulted early on in the loading stage. This quantifies the dominant effect of interfilamentous voids (or any serious defects that accrue during printing) over the presence of small volumes of fibers. This result also shows that although the addition of small volumes of steel fiber improves the overall compressive response of the printed specimen, the layer height has to be judiciously chosen to avoid the formation of defects such as interfilamentous voids which are direct results of higher layer heights used. Using a filament width that is wider than the nozzle size ensures improved overlap and void-free interfaces only when the layer heights are smaller. The results also indicate that the interlayer interfaces are not extremely critical under compression in the configuration tested; however, when the compressive strength is tested in a direction parallel to the interlayer interfaces (see [51]), then the interlayer shearing effects dominate.

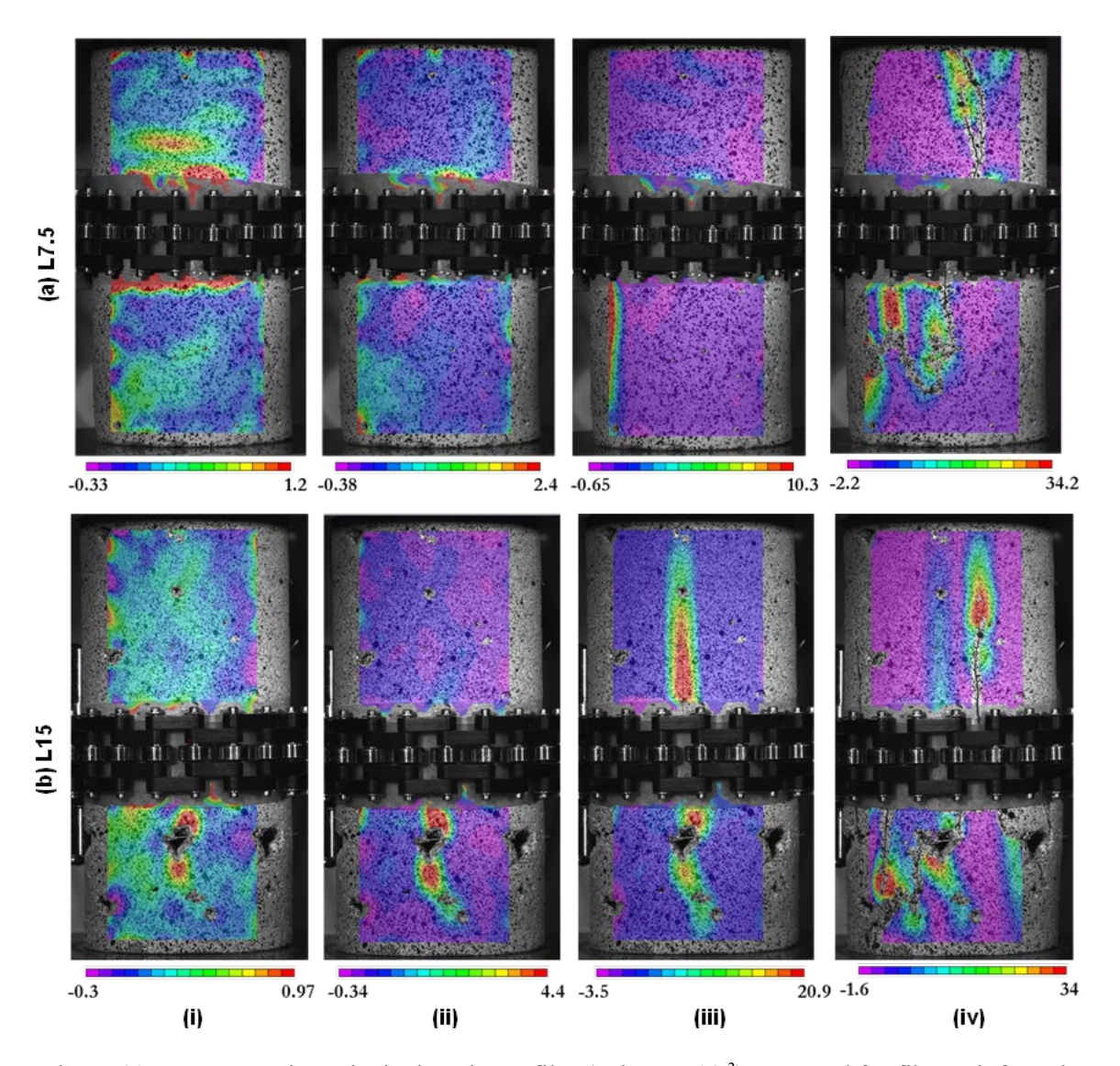


Figure 10: Representative principal strain profiles (values × 10<sup>-3</sup>) extracted for fiber-reinforced specimens with layer heights of: (a) 7.5 mm, and (b) 15 mm at four stages (from left to right) – (i) stable crack growth, (ii) unstable crack growth, (iii) peak load, and (iv) 60% residual stress at postpeak.

Crack initiation and their propagation were further observed in the prismatic specimens using 2D DIC by monitoring the orthogonal faces (left: face-1 and right: face-2), as shown in Figure 11. The three frames (from left to right) correspond to 50% peak, 90% peak, and peak stress conditions. Since the tests on prisms were not carried out under displacement controlled conditions, post-peak information is not available here. Figures 11(a) and (b) show the DIC strain profiles for the plain and fiber-reinforced L7.5 specimens, while Figures 11 (c) and (d) demonstrate the same for L15 specimens. When the prismatic specimens are extracted (see Figure 3), face-1 is perpendicular to the print direction (i.e., both interlayer and inter-filament interfaces are situated along the height of the specimen) and face-2 is along the print direction (i.e., only interlayer interfaces are situated in this plane). Thus, one can notice stress concentrations along the specimen height,

attributable to the inter-filament interfaces, as shown in 11(c) and (d). From Figure 11(c) for the L15 specimen, it can be seen that the vertical strain paths coalesce into a larger crack on one edge at 90% of peak load, and causes sudden failure at the peak load, as is evident from face-1 of the third frame in this figure. For the fiber-reinforced specimens, interfilamentous strain concentrations and cracking are observed again, which evolve into multiple cracking and propagation at 90% peak and at peak stresses. The few horizontal strain concentrations noticed in face-2 of the unreinforced specimens likely correspond to crack deviations along interfaces, which could have nucleated from a larger defect.

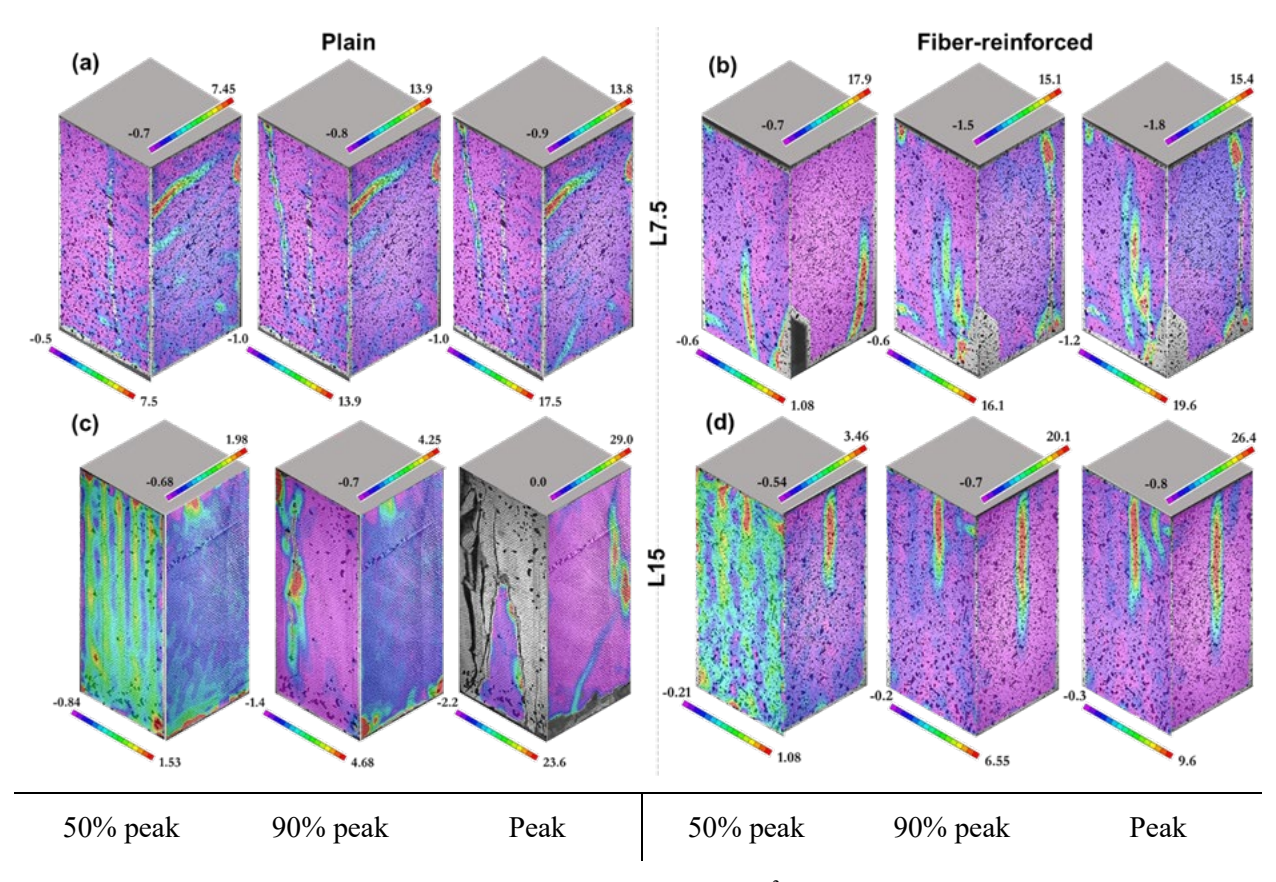


Figure 1: Representative principal strain profiles (values  $\times$  10<sup>-3</sup>) extracted for plain (a and c) and fiber reinforced (b and d) prismatic specimens on orthogonal faces using DIC for both layer heights (a and b for L7.5, and c and d for L15).

# 4 Summary and conclusions

A comprehensive evaluation of the constitutive response and failure propagation in compression of plain and fiber-reinforced 3D printed concrete specimens having different layer heights has been carried out in this study. The results reported here do not consider varying mixture formulations, nor a range of print parameters other than layer height, both in terms of layer/nozzle geometry or printing rate. The tests were carried out on cylindrical and prismatic specimens cored/cut out from vertical wall elements so that the compressive stress was applied along the direction of the wall build-up. Two different layer heights (7.5

mm and 15 mm) and one fiber volume fraction was investigated. The relationship between compressive stress and axial and radial strains were used to extract characteristic stresses, while digital image correlation (DIC) was used to examine crack propagation patterns under compression as a function of layer height.

The 3D printed specimens with a smaller layer height showed higher compressive strengths. For the higher layer height (15 mm), the plain and fiber-reinforced mortars demonstrated similar strengths, while at the lower layer height (7.5 mm), the fiber-reinforced specimen demonstrated a ~15% higher compressive strength. The stress-strain (axial and radial) relationships of the specimens with different layer heights, along with the calculated volumetric strains, were used to extract critical stress states – crack initiation stress and crack damage stress – based on four distinct phases in the pre-peak response. Stable crack growth was noted to occur at ~50-70% of the peak stress, while at ~80-95% of the peak stress, crack coalescence and propagation occurred. For both the plain and fiber-reinforced concretes, crack initiation was found to occur at a higher stress for a lower layer height. The crack damage and peak stresses were different only by ~10% for the plain and fiber-reinforced specimens having a lower layer height, but the corresponding difference was ~20% in the case of larger layer heights.

The fiber length used in this study (13 mm) was in between the two layer heights used, thereby influencing the dispersion and orientation differently, which was evident in the peak strength as well as the extracted stress states. DIC analysis also showed more prominent strain concentrations when higher layer heights were used, once again demonstrating the effects of layer height on crack propagation and failure under compression. DIC analysis on cylindrical and prismatic specimens also revealed the dominant effect of inter-filament interfaces on the crack propagation response, which was more prominent than the effect of interlayer interfaces and fiber reinforcement, when tested in the direction along the layer build-up – i.e., interlayer interfaces being perpendicular to the direction of applied load. This work has shown that accounting for layer heights, and consideration of its potential impacts on failure propagation and engineering properties are important aspects in designing 3D printed concrete structural elements.

### 5 Acknowledgements

The authors sincerely acknowledge the support from U.S. National Science Foundation (OISE: 2020095) towards this project. The authors also acknowledge the support from Salt River Materials Group, Omya, and BASF in donating the materials, and the use of 3D printing and material characterization facilities within the Laboratory for the Science of Sustainable Infrastructural Materials (LS-SIM) at Arizona State University in the completion of this project.

#### 6 References

- [1] B. Khoshnevis, Automated construction by contour crafting—related robotics and information technologies, Autom. Constr. 13 (2004) 5–19. https://doi.org/10.1016/j.autcon.2003.08.012.
- [2] G. De Schutter, K. Lesage, V. Mechtcherine, V.N. Nerella, G. Habert, I. Agusti-Juan, Vision of 3D printing with concrete Technical, economic and environmental potentials, Cem. Concr. Res. 112 (2018) 25–36. https://doi.org/10.1016/j.cemconres.2018.06.001.
- [3] H. Chen, D. Zhang, P. Chen, N. Li, A. Perrot, A Review of the Extruder System Design for Large-Scale Extrusion-Based 3D Concrete Printing, Materials. 16 (2023) 2661. https://doi.org/10.3390/ma16072661.
- [4] G.H. Ahmed, N.H. Askandar, G.B. Jumaa, A review of largescale 3DCP: Material characteristics, mix design, printing process, and reinforcement strategies, Structures. 43 (2022) 508–532. https://doi.org/10.1016/j.istruc.2022.06.068.
- [5] R. Jayathilakage, P. Rajeev, J. Sanjayan, Rheometry for Concrete 3D Printing: A Review and an Experimental Comparison, Buildings. 12 (2022) 1190. https://doi.org/10.3390/buildings12081190.
- [6] R.A. Buswell, W.R. Leal de Silva, S.Z. Jones, J. Dirrenberger, 3D printing using concrete extrusion: A roadmap for research, Cem. Concr. Res. 112 (2018) 37–49. https://doi.org/10.1016/j.cemconres.2018.05.006.
- [7] M.R. Khosravani, A. Haghighi, Large-Scale Automated Additive Construction: Overview, Robotic Solutions, Sustainability, and Future Prospect, Sustainability. 14 (2022) 9782. https://doi.org/10.3390/su14159782.
- [8] R.J.M. Wolfs, F.P. Bos, T.A.M. Salet, Hardened properties of 3D printed concrete: The influence of process parameters on interlayer adhesion, Cem. Concr. Res. 119 (2019) 132–140. https://doi.org/10.1016/j.cemconres.2019.02.017.
- [9] B. Panda, N.A. Noor Mohamed, S.C. Paul, G.V.P. Bhagath Singh, M.J. Tan, B. Šavija, The Effect of Material Fresh Properties and Process Parameters on Buildability and Interlayer Adhesion of 3D Printed Concrete, Materials. 12 (2019) 2149. https://doi.org/10.3390/ma12132149.
- [10] S.A.O. Nair, A. Tripati, N. Neithalath, Examining layer height effects on the flexural and fracture response of plain and fiber-reinforced 3D-printed beams, Cem. Concr. Compos. 124 (2021) 104254. https://doi.org/10.1016/j.cemconcomp.2021.104254.

- [11] D. Asprone, C. Menna, F.P. Bos, T.A.M. Salet, J. Mata-Falcón, W. Kaufmann, Rethinking reinforcement for digital fabrication with concrete, Cem. Concr. Res. 112 (2018) 111–121. https://doi.org/10.1016/j.cemconres.2018.05.020.
- [12] J.J. Assaad, A. Abou Yassin, F. Alsakka, F. Hamzeh, A Modular Approach for Steel Reinforcing of 3D Printed Concrete—Preliminary Study, Sustainability. 12 (2020) 4062. https://doi.org/10.3390/su12104062.
- [13] F. Bos, Z. Ahmed, E. Jutinov, T. Salet, Experimental Exploration of Metal Cable as Reinforcement in 3D Printed Concrete, Materials. 10 (2017) 1314. https://doi.org/10.3390/ma10111314.
- [14] A.R. Arunothayan, B. Nematollahi, R. Ranade, S.H. Bong, J. Sanjayan, Development of 3D-printable ultra-high performance fiber-reinforced concrete for digital construction, Constr. Build. Mater. 257 (2020) 119546. https://doi.org/10.1016/j.conbuildmat.2020.119546.
- [15] M. Hambach, M. Rutzen, D. Volkmer, Properties of 3D-Printed Fiber-Reinforced Portland Cement Paste, in: 3D Concr. Print. Technol., Elsevier, 2019: pp. 73–113. https://doi.org/10.1016/B978-0-12-815481-6.00005-1.
- [16] Y.-C. Wu, M. Li, Effects of Early-Age rheology and printing time interval on Late-Age fracture characteristics of 3D printed concrete, Constr. Build. Mater. 351 (2022) 128559. https://doi.org/10.1016/j.conbuildmat.2022.128559.
- [17] G. Ma, Z. Li, L. Wang, F. Wang, J. Sanjayan, Mechanical anisotropy of aligned fiber reinforced composite for extrusion-based 3D printing, Constr. Build. Mater. 202 (2019) 770–783. https://doi.org/10.1016/j.conbuildmat.2019.01.008.
- [18] B. Panda, S. Chandra Paul, M. Jen Tan, Anisotropic mechanical performance of 3D printed fiber reinforced sustainable construction material, Mater. Lett. 209 (2017) 146–149. https://doi.org/10.1016/j.matlet.2017.07.123.
- [19] M. van den Heever, F. Bester, J. Kruger, G. van Zijl, Mechanical characterisation for numerical simulation of extrusion-based 3D concrete printing, J. Build. Eng. 44 (2021) 102944. https://doi.org/10.1016/j.jobe.2021.102944.
- [20] V.V. Ingle, S.K. Kaliyavaradhan, P.S. Ambily, D. Shekar, 3D printable concrete without chemical admixtures: Fresh and hardened properties, Struct. Concr. (2023) suco.202300267. https://doi.org/10.1002/suco.202300267.

- [21] B. Zhu, Y. Wang, J. Sun, Y. Wei, H. Ye, H. Zhao, X. Wang, An experimental study on the influence of waste rubber particles on the compressive, flexural and impact properties of 3D printable sustainable cementitious composites, Case Stud. Constr. Mater. 19 (2023) e02607. https://doi.org/10.1016/j.cscm.2023.e02607.
- [22] D. Heras Murcia, M. Genedy, M.M. Reda Taha, Examining the significance of infill printing pattern on the anisotropy of 3D printed concrete, Constr. Build. Mater. 262 (2020) 120559. https://doi.org/10.1016/j.conbuildmat.2020.120559.
- [23] A. Tripathi, S. Nair, H. Chauhan, N. Neithalath, Print geometry alterations and layer staggering to enhance the mechanical properties of plain and fiber-reinforced 3D printed concrete (Submitted.), Am. Concr. Inst. (2023).
- [24] M. Bi, L. Xia, P. Tran, Z. Li, Q. Wan, L. Wang, W. Shen, G. Ma, Y.M. Xie, Continuous contourzigzag hybrid toolpath for large format additive manufacturing, Addit. Manuf. 55 (2022) 102822. https://doi.org/10.1016/j.addma.2022.102822.
- [25] B. Nematollahi, P. Vijay, J. Sanjayan, A. Nazari, M. Xia, V. Naidu Nerella, V. Mechtcherine, Effect of Polypropylene Fibre Addition on Properties of Geopolymers Made by 3D Printing for Digital Construction, Materials. 11 (2018) 2352. https://doi.org/10.3390/ma11122352.
- [26] P. Shakor, S. Nejadi, G. Paul, A Study into the Effect of Different Nozzles Shapes and Fibre-Reinforcement in 3D Printed Mortar, Materials. 12 (2019) 1708. https://doi.org/10.3390/ma12101708.
- [27] M. Hambach, M. Rutzen, D. Volkmer, Chapter 5 Properties of 3D-Printed Fiber-Reinforced Portland Cement Paste, in: J.G. Sanjayan, A. Nazari, B. Nematollahi (Eds.), 3D Concr. Print. Technol., Butterworth-Heinemann, 2019: pp. 73–113. https://doi.org/10.1016/B978-0-12-815481-6.00005-1.
- [28] S.A. Nair, H. Alghamdi, A. Arora, I. Mehdipour, G. Sant, N. Neithalath, Linking fresh paste microstructure, rheology and extrusion characteristics of cementitious binders for 3D printing, J. Am. Ceram. Soc. 102 (2019) 3951–3964. https://doi.org/10.1111/jace.16305.
- [29] A. Tripathi, S.A.O. Nair, N. Neithalath, A comprehensive analysis of buildability of 3D-printed concrete and the use of bi-linear stress-strain criterion-based failure curves towards their prediction, Cem. Concr. Compos. 128 (2022) 104424. https://doi.org/10.1016/j.cemconcomp.2022.104424.
- [30] A. Arora, Y. Yao, B. Mobasher, N. Neithalath, Fundamental insights into the compressive and flexural response of binder- and aggregate-optimized ultra-high performance concrete (UHPC), Cem. Concr. Compos. 98 (2019) 1–13. https://doi.org/10.1016/j.cemconcomp.2019.01.015.

- [31] C09 Committee, Test Method for Pulse Velocity Through Concrete, ASTM International, n.d. https://doi.org/10.1520/C0597-16.
- [32] K. Komloš, S. Popovics, T. Nürnbergerová, B. Babál, J.S. Popovics, Ultrasonic pulse velocity test of concrete properties as specified in various standards, Cem. Concr. Compos. 18 (1996) 357–364. https://doi.org/10.1016/0958-9465(96)00026-1.
- [33] I.O. Yaman, G. Inci, H.M. Aktan, Ultrasonic Pulse Velocity in Concrete Using Direct and Indirect Transmission, ACI Mater. J. 98 (2001). https://doi.org/10.14359/10843.
- [34] P. Wiciak, G. Cascante, M. Polak, Geometric Effects on Ultrasonic Pulse Velocity, (2017).
- [35] R. Jones, I. Fącąoaru, Recommendations for testing concrete by the ultrasonic pulse method, Matér. Constr. 2 (1969) 275–284. https://doi.org/10.1007/BF02475162.
- [36] K. Komloš, S. Popovics, T. Nürnbergerová, B. Babál, J.S. Popovics, Ultrasonic pulse velocity test of concrete properties as specified in various standards, Cem. Concr. Compos. 18 (1996) 357–364. https://doi.org/10.1016/0958-9465(96)00026-1.
- [37] S. Das, M. Aguayo, V. Dey, R. Kachala, B. Mobasher, G. Sant, N. Neithalath, The fracture response of blended formulations containing limestone powder: Evaluations using two-parameter fracture model and digital image correlation, Cem. Concr. Compos. 53 (2014) 316–326. https://doi.org/10.1016/j.cemconcomp.2014.07.018.
- [38] S. Choi, S.P. Shah, Measurement of deformations on concrete subjected to compression using image correlation, Experimental Mechanics 37 (1997) 307-313.
- [39] G.F. Bomarito, J.D. Hochhalter, T.J. Ruggles, A.H. Cannon, Increasing accuracy and precision of digital image correlation through pattern optimization, Opt. Lasers Eng. 91 (2017) 73–85. https://doi.org/10.1016/j.optlaseng.2016.11.005.
- [40] B. Pan, Digital image correlation for surface deformation measurement: historical developments, recent advances and future goals, Meas. Sci. Technol. 29 (2018) 082001. https://doi.org/10.1088/1361-6501/aac55b.
- [41] N. McCormick, J. Lord, Digital Image Correlation, Mater. Today. 13 (2010) 52–54. https://doi.org/10.1016/S1369-7021(10)70235-2.
- [42] T.C. Chu, W.F. Ranson, M.A. Sutton, Applications of digital-image-correlation techniques to experimental mechanics, Exp. Mech. 25 (1985) 232–244. https://doi.org/10.1007/BF02325092.

- [43] S. Das, A. Kizilkanat, N. Neithalath, Crack propagation and strain localization in metallic particulate-reinforced cementitious mortars, Mater. Des. 79 (2015) 15–25. https://doi.org/10.1016/j.matdes.2015.04.038.
- [44] S. Das, D. Stone, B. Mobasher, N. Neithalath, Strain energy and process zone based fracture characterization of a novel iron carbonate binding material, Eng. Fract. Mech. 156 (2016) 1–15. https://doi.org/10.1016/j.engfracmech.2016.01.024.
- [45] X. Wang, J. Wang, S.M.S. Kazmi, Y.-F. Wu, Development of new layered compression casting approach for concrete, Cem. Concr. Compos. 134 (2022) 104738. https://doi.org/10.1016/j.cemconcomp.2022.104738.
- [46] P. Carneau, R. Mesnil, N. Ducoulombier, N. Roussel, O. Baverel, Characterisation of the Layer Pressing Strategy for Concrete 3D Printing, in: RILEM Int. Conf. Concr. Digit. Fabr., Springer, 2020: pp. 185–195. https://doi.org/10.1007/978-3-030-49916-7 19.
- [47] C.D. Martin, N.A. Chandler, The progressive fracture of Lac du Bonnet granite, Int. J. Rock Mech. Min. Sci. Geomech. Abstr. 31 (1994) 643–659. https://doi.org/10.1016/0148-9062(94)90005-1.
- [48] A. Arora, A. Almujaddidi, F. Kianmofrad, B. Mobasher, N. Neithalath, Material design of economical ultra-high performance concrete (UHPC) and evaluation of their properties, Cem. Concr. Compos. 104 (2019) 103346. https://doi.org/10.1016/j.cemconcomp.2019.103346.
- [49] J. Du, W. Meng, K.H. Khayat, Y. Bao, P. Guo, Z. Lyu, A. Abu-obeidah, H. Nassif, H. Wang, New development of ultra-high-performance concrete (UHPC), Compos. Part B Eng. 224 (2021) 109220. https://doi.org/10.1016/j.compositesb.2021.109220.
- [50] J.S. Popovics, J. Zemajtis, I. Shkolnik, A study of static and dynamic modulus of elasticity of concrete, ACI-CRC Final Rep. (2008), pp. 16.
- [51] S. Surehali, A. Tripathi, N. Neithalath, Anisotropy in additively manufactured concrete specimens under compressive loading Quantification of the effects of layer height and fiber reinforcement, Materials, 16(15) (2023). https://doi.org/10.3390/ma16155488